



# The Cenozoic Seawater Conundrum: New constraints from Mg isotopes in island dolostones



Zhongya Hu<sup>a,b</sup>, Zhiqiang Shi<sup>c</sup>, Gaojun Li<sup>d</sup>, Zhiguang Xia<sup>a</sup>, Liang Yi<sup>b</sup>, Chuan Liu<sup>a</sup>, Weiqliang Li<sup>a,e,\*</sup>

<sup>a</sup> State Key Laboratory for Mineral Deposits Research, School of Earth Sciences and Engineering, Nanjing University, Nanjing, Jiangsu 210093, China

<sup>b</sup> State Key Laboratory of Marine Geology, Tongji University, Shanghai 200092, China

<sup>c</sup> State Key Laboratory of Oil and Gas Reservoir Geology and Exploitation, Chengdu University of Technology, Chengdu, Sichuan 610059, China

<sup>d</sup> MOE Key Laboratory of Surficial Geochemistry, School of Earth Sciences and Engineering, Nanjing University, Nanjing, Jiangsu 210093, China

<sup>e</sup> Frontiers Science Center for Critical Earth Material Cycling, Nanjing University, China

## ARTICLE INFO

### Article history:

Received 23 December 2021

Received in revised form 23 July 2022

Accepted 27 July 2022

Available online xxxx

Editor: A. Jacobson

### Keywords:

Cenozoic seawater

Mg isotopes

Mg/Ca ratios

dolostone

Xisha Islands

## ABSTRACT

The Mg/Ca ratio of seawater increased from ~1.5 to its present value of 5.4 over the Neogene, indicating a fundamental imbalance in the Mg–Ca cycle during the late Cenozoic. The imbalance in Mg–Ca cycles since the late Cenozoic, however, is contrasted by an arguable constancy in the Mg isotope compositions of seawater ( $\delta^{26}\text{Mg}_{\text{sw}}$ ) reconstructed from several low-resolution carbonate records. Addressing such Cenozoic Seawater Conundrum requires reliable seawater Mg isotopic records. The Xisha Islands in the South China Sea host large Cenozoic dolostone sequences that record seawater chemistry over the past 23 Myr. This study reports the Mg isotopic and trace elemental compositions of island dolostones in the well-studied Xike-1 drill core from the Xisha Islands. Petrographic, C–O–Sr isotopic, and paleomagnetic data from the drill core samples collectively support a “fluid-buffered”, syn-depositional origin for the dolostones. The dolostones from the Xike-1 core have a narrow range of  $\delta^{26}\text{Mg}$  ( $-2.83\text{‰} \pm 0.12\text{‰}$ ), confirming that  $\delta^{26}\text{Mg}_{\text{sw}}$  have been stable around the modern value ( $-0.83\text{‰}$ ) since the late Cenozoic. This record provides a new opportunity to better understand the Mg–Ca cycle during the late Cenozoic. We ran numerical models of global seawater Mg–Ca contents and  $\delta^{26}\text{Mg}_{\text{sw}}$  with the most recently published flux and isotope fractionation data. The results show that the contrast between the constancy of  $\delta^{26}\text{Mg}_{\text{sw}}$  values and the dramatic increase in seawater Mg/Ca ratios cannot be explained by a single mechanism (i.e., a decrease in the rate of phyllosilicate formation on the seafloor alone). Instead, processes involving different Mg fluxes need to be coupled to explain the observed trends in Mg content and isotopic compositions of Cenozoic seawater. The solution to the Cenozoic Seawater Conundrum includes simultaneous decreases in the rates of both clay formation and dolomitization on the seafloor, or an increase in the rate of both continental weathering together with decreased seafloor clay formation. Our study underlines the sensitivity of the Mg cycle to the interactions between climate, continental weathering, and seafloor processes during the late Cenozoic.

© 2022 Elsevier B.V. All rights reserved.

## 1. Introduction

Seawater chemistry has changed dramatically during the Cenozoic (Caves et al., 2016; Coggon et al., 2010; Horita et al., 2002; Lowenstein et al., 2001). In particular, the Mg/Ca ratio increased from 1.5 to 5.4 during the long-term cooling of the Earth's climate that occurred from the Neogene (Coggon et al., 2010; Horita et al., 2002; Lowenstein et al., 2001), reflecting striking changes in the global Mg and Ca cycles of the Earth system. The cause of

the observed rise in seawater Mg/Ca ratios during the Cenozoic remains enigmatic, with different hypotheses proposed, including a decrease in the rate of seafloor spreading (Coggon et al., 2010), a decline in the intensity of marine dolomitization (Wilkinson and Algeo, 1989), an increase in continental weathering (Li and Elderfield, 2013), and reduced removal of Mg by phyllosilicates (Dunlea et al., 2017). Surficial cycling of Mg involves the weathering of continental rocks, carbonate precipitation, and reverse weathering on the seafloor. The Mg isotope compositions of marine carbonates, river water, authigenic clay, and weathering products are highly variable (Teng, 2017). The large fractionation of Mg isotopes in low-temperature systems makes Mg isotopes an effective tracer of

\* Corresponding author.

E-mail address: liweiqliang@nju.edu.cn (W. Li).

the surficial Mg cycle (Higgins and Schrag, 2015; Hu et al., 2021; Liu et al., 2014; Pogge von Strandmann et al., 2014), and the Mg isotope compositions of seawater could respond to changes in the global Mg cycle (Li et al., 2015; Tipper et al., 2006). Efforts have been made to constrain the Mg isotope compositions of Cenozoic seawater ( $\delta^{26}\text{Mg}_{\text{sw}}$ ) using various Mg-bearing biogenic carbonates. Higgins and Schrag (2015) and Gothmann et al. (2017) argued that the  $\delta^{26}\text{Mg}_{\text{sw}}$  has increased by  $\sim 0.2\text{‰}$  since the Neogene. In contrast, Pogge von Strandmann et al. (2014) suggested that the  $\delta^{26}\text{Mg}$  of Cenozoic seawater decreased rapidly from  $0.2\text{‰}$  to  $-0.82\text{‰}$ . The inconsistency in the biogenic carbonate Mg isotope records complicates the study of changes in Cenozoic seawater chemistry using Mg isotopes. Alternative and robust Mg isotope records with a more complete understanding of the proxies, and more detailed modelings are needed to resolve the Cenozoic Seawater Conundrum.

Marine dolomite is a major sink for seawater Mg (Li et al., 2015; Tipper et al., 2006). Although the dolomitization process can vary in marine environments (Warren, 2000) and the Mg isotope response to dolomitization could also vary between different systems (Ahm et al., 2018; Geske et al., 2015; Higgins et al., 2018), the processes of pervasive marine dolomitization tend to be fluid- (or seawater-) buffered (Ahm et al., 2018; Higgins et al., 2018). Specifically, the advective transport of Mg dominates in shallow carbonate shelf systems, where the rate of fluid flow within pervasive dolomitization systems is high relative to the rate of reaction and diffusion, leading to short residence times for Mg in pore fluids (Fantle and Higgins, 2014; Fantle et al., 2020). Under these conditions (i.e., an advection dominated regime), dolostones commonly possess  $\delta^{26}\text{Mg}$  values that are in equilibrium with coeval seawater (Ahm et al., 2018; Higgins et al., 2018). The robustness of the Mg isotope compositions of dolostones against post-depositional processes, including dissolution in groundwater, early diagenesis, burial metamorphism, and hydrothermal alteration, has been well established (Fantle and Higgins, 2014; Fantle et al., 2020; Geske et al., 2012; Jacobson et al., 2010). As an emerging proxy, the Mg isotope compositions of dolostones have been applied to the study of marine events of different spatial and temporal scales, including transient restriction events in the Paleo-Tethys Ocean at the end of the Permian (Hu et al., 2021), eustatic sea level changes on carbonate platforms (Bialik et al., 2018), and Cryogenian deglaciation (Liu et al., 2014).

Cenozoic carbonates are generally characterized by a lack of extensive marine dolomitization (Budd, 1997; Li et al., 2021); however, the climatic and hydrological conditions on tropical reef islands can promote fluxing of warm, Mg-rich fluids within carbonate sequences, which leads to the formation of massive dolostones (Budd, 1997; Warren, 2000). The formation of thick dolostone units on tropical reef islands continued during the Cenozoic, despite a general paucity of marine dolomitization in recent geological times (i.e., the “dolomite problem”; Budd, 1997; Warren, 2000). Cenozoic island dolostones formed mostly through pervasive dolomitization and have not been subjected to complicated burial diagenesis (Budd, 1997). On isolated islands, seawater is the only available source of Mg for dolomitization (Budd, 1997; Shi et al., 2016; Wang et al., 2018); therefore, massive dolostones on tropical islands can potentially serve as an Mg isotopic archive for Cenozoic seawater.

Since the 1970s, scientific and oil exploration drilling in the South China Sea revealed massive Cenozoic dolostone successions in the Xisha Islands (Budd, 1997; Shi et al., 2016; Wang et al., 2018). A complete sequence of late Cenozoic carbonate rocks that were deposited on metamorphic basement was recovered from drill core Xike-1 (XK-1) (Shi et al., 2016). The stratigraphic chronology of the drill core has been well-constrained by magnetostratigraphy, biostratigraphy, and  $^{87}\text{Sr}/^{86}\text{Sr}$  chemostratigraphy (Bi et al.,

2018b; Shao et al., 2017; Yi et al., 2018). The dolostone samples in the XK-1 core provide a unique Mg isotope record that can be used to study the history of Mg isotopic compositions during the late Cenozoic and shed new light on Mg–Ca cycling during the late Cenozoic.

## 2. Sample descriptions and methods

### 2.1. Geological setting and the XK-1 drill core

The South China Sea is the largest marginal sea of the western Pacific Ocean. The Xisha Islands are located on an elevated submarine plateau in the northwest of the South China Sea (Fig. 1A) and are composed of a group of atolls (Fig. 1B) (Shao et al., 2017; Wang et al., 2018). The basement of the islands drifted southward from the South China continental block during the late Eocene to early Oligocene and was submerged from late Oligocene onwards (Shao et al., 2017; Wang et al., 2018). Tropical carbonate platforms developed since the early Miocene and flourished during the middle–late Miocene (Wang et al., 2018).

The carbonate sequences in the Xisha Islands can be divided into five units based on their lithology (Shi et al., 2016): the Sanya Formation (early Miocene), the Meishan Formation (middle Miocene), the Huangliu Formation (late Miocene), the Yinggehai Formation (Pliocene), and the Ledong Formation (Pleistocene–Holocene). The Huangliu Formation and Sanya Formation are dominated by massive dolostones of  $\sim 200$  m thick that extend laterally for  $>50$  km (Fig. 1C and 2). The Meishan Formation and the lower part of the Yinggehai Formation are variably dolomitized (Fig. 2). In the upper part of the Yinggehai Formation and the Ledong Formation, the dolomite contents are mostly  $<10\%$ , particularly in the Ledong Formation, which is composed of almost pure limestone (Bi et al., 2018a; Shao et al., 2017) (Appendix 2 Fig. S2-1). The carbonate sequences are typical reef carbonate in forms of packstone and wackestone (Shao et al., 2017; Wang et al., 2018).

The development of carbonate platform in the Xisha Islands was correlated with eustatic sea level changes (Shao et al., 2017). Deposition of tropical carbonates on the basement began during the early Miocene (ca. 23 Ma) owing to basin-wide tectonic subsidence and sea-level rise (Shao et al., 2017; Wang et al., 2018). Since the end of the middle-Miocene climate optimum (17–15 Ma), the expansion of the Antarctic ice sheet caused a long-term drop in sea level, which significantly reduced the habitat of shallow-water benthonic organisms and impeded the development of the reef (Shao et al., 2017). The onset of the South Asian Monsoon at 12.9 Ma led to a “warm pool” in the South China Sea, and the relatively habitable marine environment and the rise in regional sea level promoted the propagation of reef-forming organisms and the expansion of the carbonate platform in the Xisha Islands (Fig. 2; Shao et al., 2017; Shi et al., 2016). Global cooling and regional tectonic subsidence since the late Pliocene resulted in another drop in sea level, and the shallow carbonate underwent meteoric dissolution and erosion (Shao et al., 2017). In the Xisha Islands, dolomitization generally occurred when the sea level was high (Shao et al., 2017; Wang et al., 2018). During these stages, the platform expanded rapidly, facilitating the formation of lagoons. The pervasive dolomitization in the Xisha Islands has been attributed to flows of hypersaline seawater percolating from the lagoons in the carbonate platform out toward its rim and slope (Bi et al., 2018a). The limestones, which formed during lowstands, underwent different degrees of meteoric diagenesis (Shi et al., 2016).

The XK-1 core is 1268 m long and was drilled from Shi Island in the Xuande Atoll, Xisha Islands (Fig. 1B). This drill core has been subject to comprehensive studies of carbonate sedimentology, chemostratigraphy, foraminiferal biostratigraphy, and magnetostratigraphy, which provide a complete chronostratigraphic col-

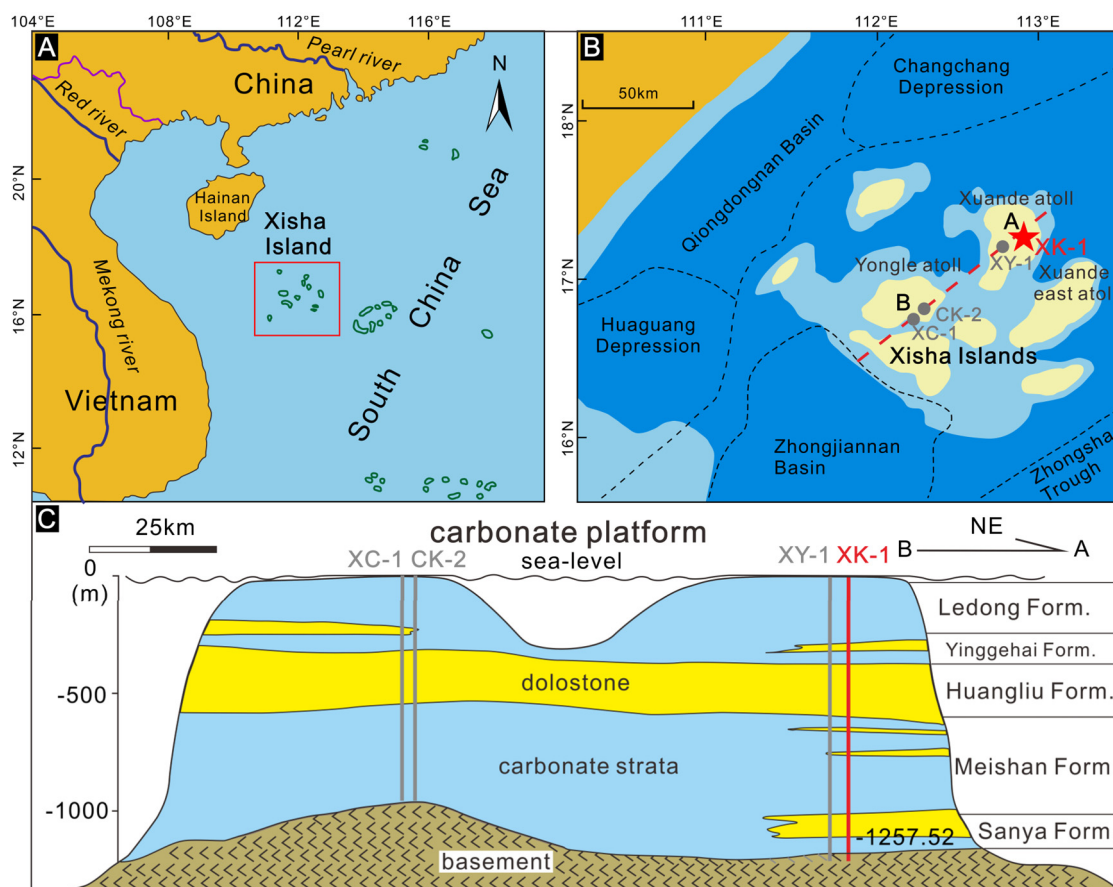


**Fig. 1.** (A) Location of the Xisha Islands in the South China Sea. (B) Map of the Xisha Islands, showing the tectonic and sedimentary framework and the site of the XK-1 core, modified from Wang et al. (2018). (C) Cross section through the carbonate platform in the Xisha Islands, showing the distribution of dolostones based on four drill cores, modified from Wang et al. (2018).

umn starting at 22.5 Ma for the Xisha Islands carbonates (Bi et al., 2018b; Shao et al., 2017; Yi et al., 2018). Sixty carbonate samples, predominantly dolostones or dolomitized limestones, were collected from the XK-1 core for this study.

## 2.2. Mineralogical characterization

Thin sections were prepared from the core samples for microscopic observation. Cathodoluminescence (CL) microscopy was performed using a Cambridge Image Technology Ltd CL8200 MK5 cold cathode instrument at Nanjing University, China. CL images were taken with an exposure time of 50 s. The rest of the samples were pulverized into powders and placed in a Rigaku Rapid II dual-source X-ray diffractometer for powder X-ray diffraction (XRD) analysis. The instrument was equipped with a rotating Mo anode target X-ray source ( $\text{Mo } K\alpha = 0.714 \text{ \AA}$ ) that was running at 40 kV and 100 mA. Diffracted X-rays were collected by an imaging plate, and 5 minutes of exposure time was used for each sample. The intensities of the (104) peak for calcite and dolomite were obtained from the XRD spectra using the Jade 6.5 software, and the relative bulk-rock abundance of dolomite and calcite was estimated from the peak intensities. The Mg contents (or stoichiometry) of calcite and dolomite were calculated based on  $d(104)$  values.

## 2.3. Trace element analysis

Forty-eight carbonate samples were selected for trace element analysis. The bulk carbonates were ground to 200 mesh in an agate mortar. About 20 mg of powder from each sample was weighed and dissolved in 5 mL of 3N  $\text{HNO}_3$  at 95 °C for 12 h, then 0.1 mL

of the dissolved sample was transferred into a pre-cleaned Teflon beaker and diluted to 15 mL using 2%  $\text{HNO}_3$ . Trace element concentrations were measured using an Agilent 7900 ICP-MS at the State Key Laboratory of Marine Geology at Tongji University, China. The analytical precision was <5% (RSD).

## 2.4. Magnesium isotope analysis

Fifty-two carbonate samples were selected for Mg isotope analysis. An aliquot of each dissolved sample that contained ~50  $\mu\text{g}$  Mg was used for Mg purification. Mg was purified using the two-stage ion exchange procedure described by Hu et al. (2021). After purification, the mass of matrix elements was <0.5% that of Mg, and the Mg recovery was >98%. Mg isotope analysis was performed using a Thermo Fisher Scientific Neptune Plus multi-collector (MC)-ICP-MS at Nanjing University. The Mg concentration of each sample was diluted to  $500 \pm 50$  ppb and analyzed against a 500 ppb in-house Mg isotope standard solution using standard-sample-standard bracketing. The analytical accuracy of the Mg isotope measurements was verified by measuring the Cambridge1 and DSM3 international Mg isotope standards. To monitor the accuracy of the chemical procedures, the IAPSO seawater and USGS rock standards (DTS-2b, BIR-1a) were processed with samples using the same two-stage ion exchange procedures. All of the measured  $\delta^{26}\text{Mg}$  values of the standards matched the published values within 0.10‰, and most were within 0.05‰. The typical internal precision (2 standard error) was <0.04‰ for  $^{26}\text{Mg}/^{24}\text{Mg}$  and <0.02‰ for  $^{25}\text{Mg}/^{24}\text{Mg}$ . Based on repeat analysis of the geological standards and pure Mg solutions, the long-term external

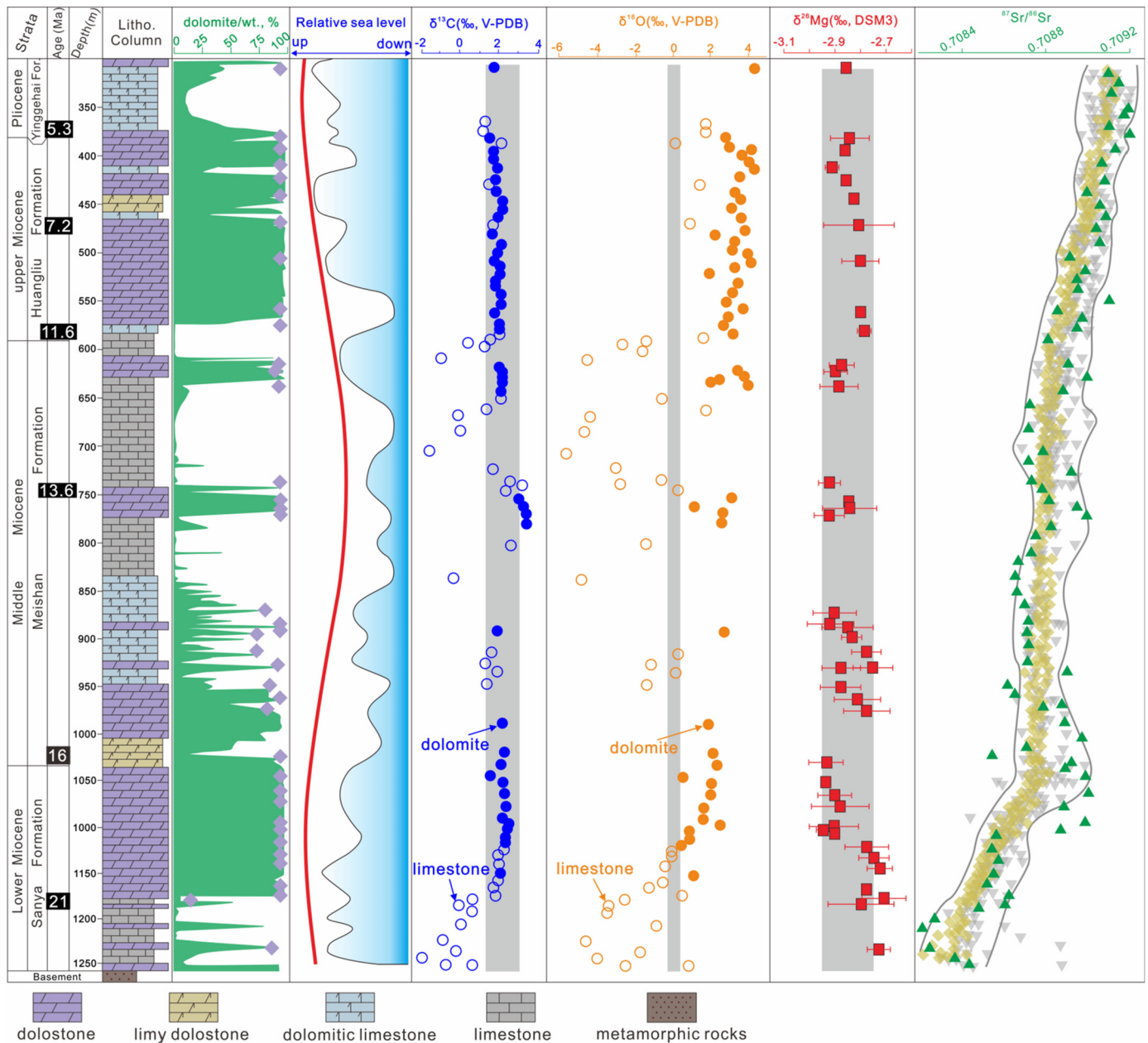


**Fig. 2.** Lithological column for the XK-1 core and stratigraphic variations in mineralogy and C–O–Mg–Sr isotopic compositions of the carbonates. Dolostones are defined as carbonates with dolomite contents of >85% and calcite contents of <15%, limy dolostones have calcite contents of 15%–50%, dolomitic limestones have calcite contents of 50%–85%, and limestones have dolomite contents of <15%. The age is constrained by biostratigraphic and chemostratigraphic data from Shao et al. (2017) and Shi et al. (2016). Continuous dolomite abundance data (filled green curve) along the drill core are from Bi et al. (2018b). Purple diamonds are the dolomite contents of the samples analyzed in this study. The eustatic sea-level curve is from Shao et al. (2017); the blue filled curve shows sea level inferred from facies analyses of carbonates in the XK-1 core, and the red curve shows the sea level in the South China Sea. C–O isotope data are from Shi et al. (2016).  $^{87}\text{Sr}/^{86}\text{Sr}$  ratios of carbonate in the XK-1 core (filled green triangles) are from Bi et al. (2018b), and grey triangles and yellow diamonds show the late Cenozoic seawater  $^{87}\text{Sr}/^{86}\text{Sr}$  ratios compiled by Bi et al. (2018b) and McArthur et al. (2001), respectively. The sampling sites for Mg isotopic analyses are mostly coincident with the sites of samples which have been selected for C–O–Sr isotope analyses. (For interpretation of the colors in the figure(s), the reader is referred to the web version of this article.)

precision and accuracy of the  $\delta^{26}\text{Mg}$  measurements were <0.10‰ at the  $2\sigma$  level.

### 3. Results

The dolostones in the XK-1 core are generally grey to white with well-developed intergranular pores (Appendix Fig. S2-1A–C). Hydrothermal minerals, including saddle dolomite, quartz, and fluorite, are absent in the pores. The limestones are mostly composed of micritic calcite (Appendix Fig. S2-1D–E) and contain numerous skeletal fossils, including foraminifera (Appendix Fig. S2-1D). The

limestone underwent dissolution to some extent during an early stage of diagenesis, as shown by the calcite rims around the dissolution pores (Appendix Fig. S2-1E). Almost all of the dolostone samples are composed of fine-crystalline dolomite (Appendix Fig. S2-1G–H). Overall, the carbonate minerals (dolomite and calcite) have a dull red luminescence in CL images, and no overgrowth and recrystallization zones are seen (Appendix Fig. S2-1F and I).

The cation ordering of the dolomite is variable, with  $I(015)/I(110)$  (the intensity ratio of diffraction peaks for the (105) and (110) planes) ranging from 0.25 to 0.47 (Fig. 3B). The  $d_{104}$  values of the dolomite are 2.893–2.907 (Fig. 3C), which is higher than



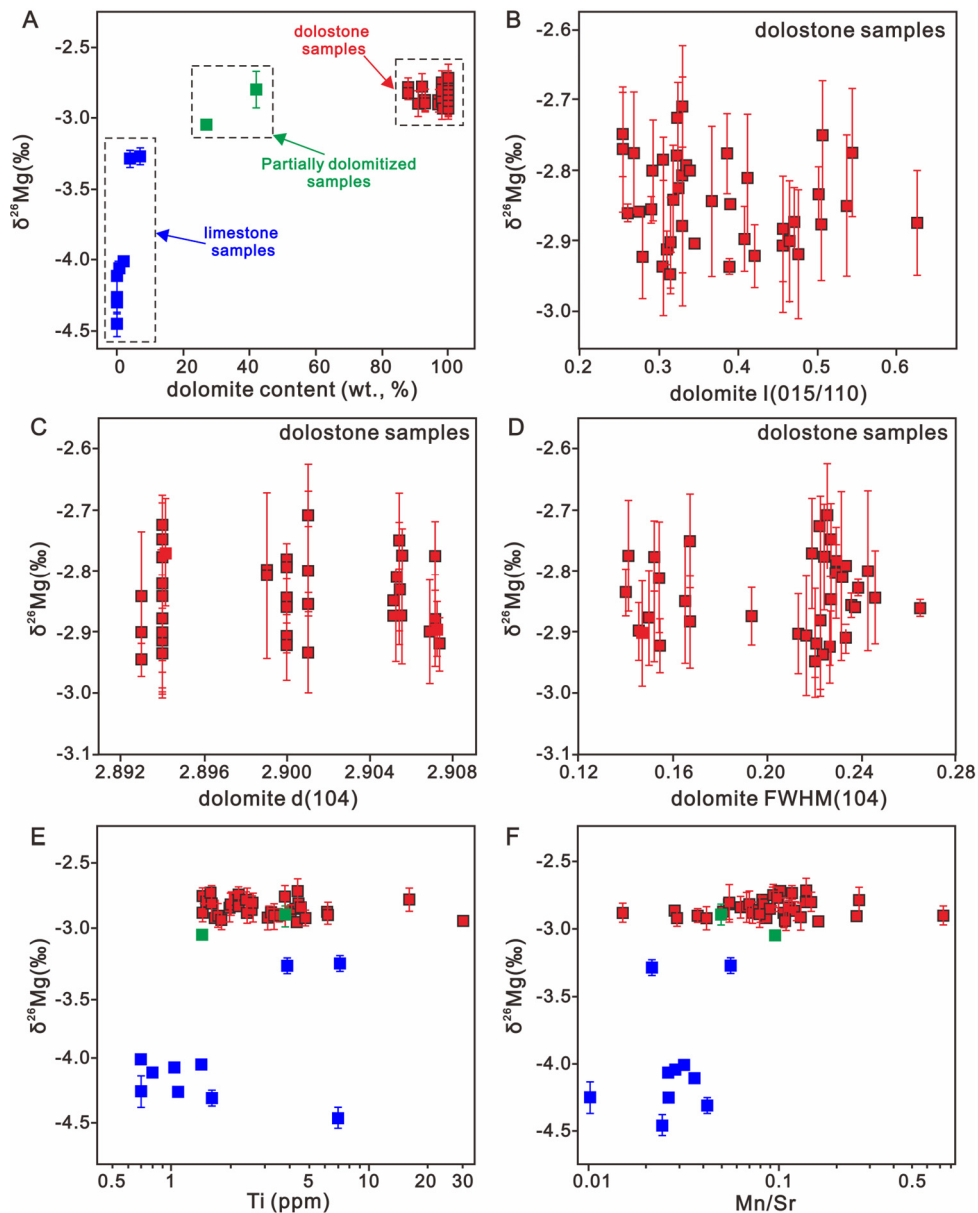


**Fig. 3.** (A) Bulk-rock  $\delta^{26}\text{Mg}$  values versus dolomite contents. (B–D)  $\delta^{26}\text{Mg}$  values versus dolomite mineralogical parameters, including (B) an index of cation ordering, (C)  $d(104)$  distance, and (D) sharpness of the (104) peak of the dolostone samples (dolomite contents > 50%). (E–F)  $\delta^{26}\text{Mg}$  values versus trace elemental contents. The blue and red squares represent the limestone which dolomite contents < 10% and the dolostone which calcite contents < 20%, the green squares represent the carbonate contain dolomite contents higher than 10% but lower than 30%.

that of stoichiometric dolomite (2.88) and corresponds to calcian dolomite with 45–48 mol.%  $\text{MgCO}_3$ . The calcite in the carbonates has a narrow range of  $d_{104}$  values (3.024–3.033, mostly 3.030) (Appendix Table S1-2), corresponding to 1.1 mol.%  $\text{MgCO}_3$  in calcite.

The limestones yield variable  $\delta^{26}\text{Mg}$  values (−4.46‰ to −3.27‰) (Fig. 3A); in contrast, the dolostone samples (dolomite contents of > 50%) have a narrow range of  $\delta^{26}\text{Mg}$  values (−2.95‰ to −2.71‰) (Fig. 2 and 3A), which are almost within an envelope by the external uncertainty of  $\pm 0.1$ ‰. The  $\delta^{26}\text{Mg}$  values are not correlated with dolomite lattice parameters (i.e., the degree of order,  $d_{104}$  values, and peak sharpness; Fig. 3B–D). This lack of variation is similar to that of published C isotope data for dolomite-dominated carbonates from the same intervals of the XK-1 core (Fig. 2).

The Ti concentrations of the carbonate samples are 0.7–30.9 ppm, with a mean value of 3.8 ppm (Appendix Table S1-3,

Fig. 3E). In general, the carbonates contain low Mn concentrations (2.5–103.7 ppm) (Appendix Table S1-3). The Sr concentrations of carbonates mostly range from 200 to 500 ppm (Appendix Table S1-3). The bulk-rock Mn/Sr ratios of the carbonates are 0.01–0.72 (Fig. 3F). The  $\delta^{26}\text{Mg}$  values of the carbonate samples are not correlated with Ti concentrations or Mn/Sr ratios (Fig. 3E–3F).

## 4. Interpretation and discussion

### 4.1. Syn-depositional origin of dolostones in the XK-1 core

A common concern with carbonate-based proxies is whether the primary signals have been overprinted. For example, recrystallization during shallow burial stage can significantly alter the crystallographic properties of dolomite crystals as well as geochemical compositions within a few hundred years since deposition (Fantle et al., 2020; Immenhauser, 2021). In the XK-1 core, dolomites

occur universally as fine crystals without overgrowth rims (Appendix Fig. S2-1G-I), and hydrothermal minerals, including saddle dolomite, quartz, and fluorite, are absent in the carbonate succession. Moreover, the carbonates have low bulk-rock Mn contents (mostly <50 ppm) (Appendix Table S1-3) and low Mn/Sr ratios (<0.7) (Fig. 3F). These are all consistent with the lack of late overprinting. C and O isotopic compositions of the dolostone samples are relatively constant along the drill core. In particular, the  $\delta^{18}\text{O}$  values of dolostones are high (mainly 0.5‰–4‰) and similar to the  $\delta^{18}\text{O}$  values of other Cenozoic marine dolostones globally (Fantle and Higgins, 2014; Higgins et al., 2018; Wang et al., 2018), whereas the calcite-dominated carbonate samples have lower  $\delta^{18}\text{O}$  values (Fig. 2). The high  $\delta^{18}\text{O}$  values of the dolostones preclude overprinting of O isotopes by diagenetic fluids such as meteoric water (Chang et al., 2020; Immenhauser, 2021). Assuming similar exchangeability of O and Mg between dolomite and fluids, the O isotope compositions of the dolostones would be more sensitive to diagenetic alteration than Mg isotope compositions due to the high O/Mg ratio of aqueous solutions (Hu et al., 2021). Therefore, the pristine O isotope signatures of the dolostone samples show that Mg isotopic compositions of dolostones must have also remained unaltered since the completion of dolomitization.

The paleomagnetic ages of the XK-1 core are consistent with the biostratigraphic ages within 0.2 Myr (Yi et al., 2018) (Appendix 2 Fig. S2-2), indicating that the thermoremanent magnetization of the dolostones was syn-depositional. If the dolomitization was triggered by late diagenetic fluid overprinting, then the magnetization would be reset (Cioppa et al., 2003), yielding younger paleomagnetic ages than the biostratigraphic ages for dolostones in the lower units. Furthermore, seawater is the only available Mg-rich source for the pervasive dolomitization of thick dolostone successions deposited in isolated islands that are surrounded by deep ocean basins (Budd, 1997; Wang et al., 2018). The  $^{87}\text{Sr}/^{86}\text{Sr}$  ratios of the samples increase upwards in the XK-1 core, from 0.7082 at the base to 0.7092 at the top (Bi et al., 2018b), which closely tracks the curve of Neogene seawater  $^{87}\text{Sr}/^{86}\text{Sr}$  ratios on time-scale of million years (Fig. 2). As such, the  $^{87}\text{Sr}/^{86}\text{Sr}$  ratios also attest to the syn-depositional origin of the carbonates. Finally, the vertical alternation between dolostone- and limestone-rich strata in the Xisha Islands (Fig. 1C) is incompatible with formation of these separated dolostone layers from a single diagenetic event. Based on the multiple lines of evidence above, we argue that the dolomites most likely formed under a syn-depositional condition.

Sedimentary facies analysis suggests that the dolostones formed mostly during periods of high sea level (Fig. 2). Bi et al. (2018a) reported that the fluid inclusions in the Xisha dolomites had relatively high  $\text{SO}_4^{2-}$  contents,  $\delta^{18}\text{O}$  values, and Br/Cl ratios, and suggested that the fluid involved in the pervasive dolomitization was concentrated seawater. On an isolated carbonate platform, similar hypersaline fluids are typically generated by the evaporation of seawater in semi-closed lagoons within the platform (Warren, 2000). In the Xisha Islands, the carbonate platform expanded significantly during sea level highstands, which were characterized by the rapid growth of the atoll reef and the development of a central lagoon (Shao et al., 2017) (Appendix Fig. S2-3). Saline brine formed by the evaporation of seawater within the lagoon could percolate downward and outward, leading to dolomitization in the carbonate platform (Shao et al., 2017; Wang et al., 2018). In such hydrological conditions, Mg isotopes in the dolostones would have been buffered by the seawater-derived brine (Fantle and Higgins, 2014; Fantle et al., 2020), which had higher ionic concentrations but the same Mg isotope compositions as coeval seawater. Therefore, the dolostones in the Xisha Islands have a fluid-buffered, syn-depositional, reflux origin, and the Mg isotope signatures of the dolostones from the XK-1 core record the Mg isotopic composition of coeval seawater over the past 23 Myr.

#### 4.2. Long-term stability of $\delta^{26}\text{Mg}_{\text{sw}}$ over the past 23 Myr

Before reconstructing the history of  $\delta^{26}\text{Mg}_{\text{sw}}$  from dolostones in the XK-1 core, we first evaluate whether contamination of terrigenous detrital materials and calcite could significantly affect the  $\delta^{26}\text{Mg}$  of the bulk dolostones. Petrographic observations and XRD analyses confirmed the absence of terrigenous detrital material in the carbonates from the XK-1 core. The carbonate samples have low Ti contents (mostly <10 ppm), and there is no correlation between  $\delta^{26}\text{Mg}$  values and Ti contents (Fig. 3E). Therefore, contamination of the carbonate Mg isotope compositions by terrigenous detritus is ruled out. The limestones have lighter Mg isotope compositions than the dolostones (Fig. 3A); however, as the calcite has Mg contents of only ~1 mol.% in its lattice, its influence on the bulk-rock Mg isotope compositions of the dolostones is negligible. A mass balance calculation for a dolostone sample that contains 80% dolomite and 20% calcite shows that <1.5% of the total Mg is hosted by the calcite. Assuming that the  $\delta^{26}\text{Mg}$  values of calcite and dolomite are about -4.10‰ and -2.83‰, respectively (i.e., the mean  $\delta^{26}\text{Mg}$  values of the two minerals in the XK-1 core), 20 wt.% calcite in a dolostone would only lower the bulk  $\delta^{26}\text{Mg}$  value by 0.03‰ relative to the value for pure dolomite (Details in Appendix 2), which is well within the analytical uncertainty (0.1‰).

Another concern is whether variations in dolomite stoichiometry affect Mg isotope fractionation, as the stoichiometry of Cenozoic island dolomite is generally more variable than Paleozoic dolomite (Budd, 1997). In the Xisha Islands, the dolomite contains 45–48 mol.%  $\text{MgCO}_3$  (calculated using dolomite  $d_{104}$  values, Appendix 1 Table S1-2); however,  $\delta^{26}\text{Mg}$  values are not correlated with dolomite  $d_{104}$  values, nor with indexes of the degree of order and crystallinity (Fig. 3C–3F), ruling out the influence of dolomite lattice parameters on the  $\delta^{26}\text{Mg}$  values of the XK-1 core.

In addition, we note that other thick late Cenozoic dolostone sequences, including the ODP site 1196 Hole A (ca. 24 Ma; Fantle and Higgins, 2014), San Salvador (ca. 6.2 Ma; Ahm et al., 2018), the GB-1 core (ca. 5.0 Ma; Higgins et al., 2018), and the WC core (ca. 5.6 Ma; Higgins et al., 2018) from the Bahamas, have  $\delta^{26}\text{Mg}$  values similar to the dolostones in the Xisha Islands (-2.95‰ to -2.71‰), despite their great geographic separation (Appendix 2 Fig. S2-3). The dolostone units in the XK-1 core and from other relevant marine systems worldwide that formed via pervasive dolomitization appear to have consistent  $\delta^{26}\text{Mg}$  values throughout the late Cenozoic.

Over the past 23 Myr, the change in average surface temperature of the oceans was <10 °C (Caves et al., 2016), which would introduce a <0.1‰ change in the equilibrium Mg isotope fractionation factor for dolomite (Li et al., 2015). Assuming a Mg isotope fractionation factor ( $\Delta^{26}\text{Mg}_{\text{dolo-sw}}$ ) of -2.0‰ for dolomitization (Fantle and Higgins, 2014; Higgins and Schrag, 2015; Li et al., 2015), the  $\delta^{26}\text{Mg}$  values of late Cenozoic seawater inferred from the records in island dolostones were about -0.95‰ to -0.71‰, with a mean value of  $-0.83 \pm 0.12$ ‰ (Fig. 4), consistent with the value of modern seawater (Teng, 2017). The  $\delta^{26}\text{Mg}$  values of dolostones do not exhibit any noticeable stratigraphic trend along the XK-1 core, demonstrating the long-term stability of  $\delta^{26}\text{Mg}_{\text{sw}}$  since at least the Neogene. For comparison,  $\delta^{26}\text{Mg}_{\text{sw}}$  reconstructed using biogenic calcite (forams) are remarkably more scattered and inconsistent between different studies (Fig. 4). The inconsistency in different records of calcareous fossils could be explained by “vital effects” during the growth of different marine calcifiers (Saenger and Wang, 2014), or by variable post-depositional overprinting to the Mg isotope signatures of low-Mg carbonates (Fantle et al., 2020). The tropical island dolostones in the XK-1 core, by contrast, are immune of “vital effects” and robust against late overprinting, and the Mg isotope data of the XK-1 reflect a constancy in  $\delta^{26}\text{Mg}_{\text{sw}}$  of  $-0.83 \pm 0.12$ ‰ over the past 23 Myr (Fig. 4).

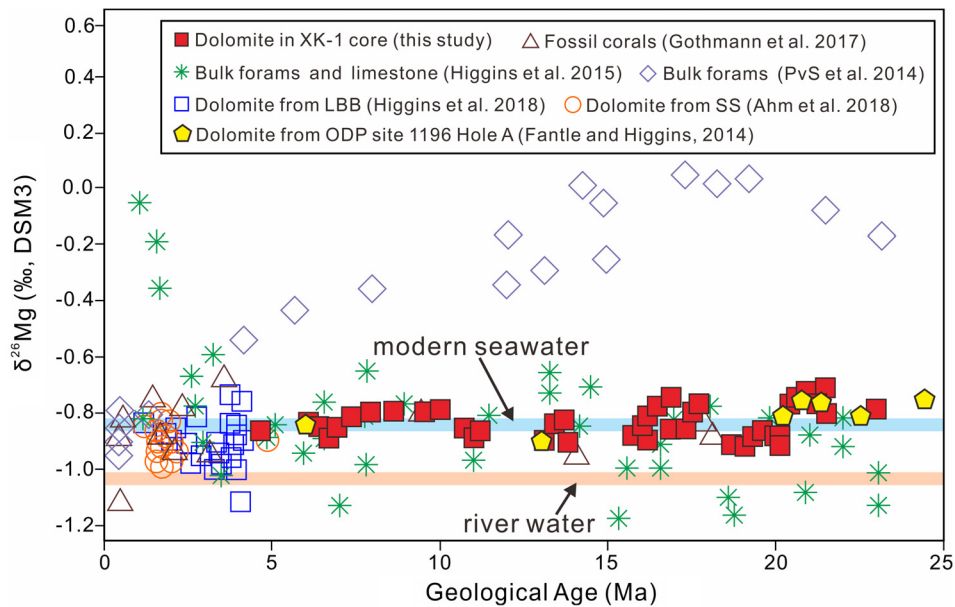


**Fig. 4.** Seawater  $\delta^{26}\text{Mg}$  values inferred from the isotope records in the island dolomite from the XK-1 core, and other archives. LBB: Little Bahama Bank, SS: San Salvador (Higgins et al., 2018; Ahm et al., 2018).  $\delta^{26}\text{Mg}$  values of corals are from Gothmann et al. (2017), and values for bulk forams are from Higgins and Schrag (2015) and Pogge von Strandmann et al. (2014).

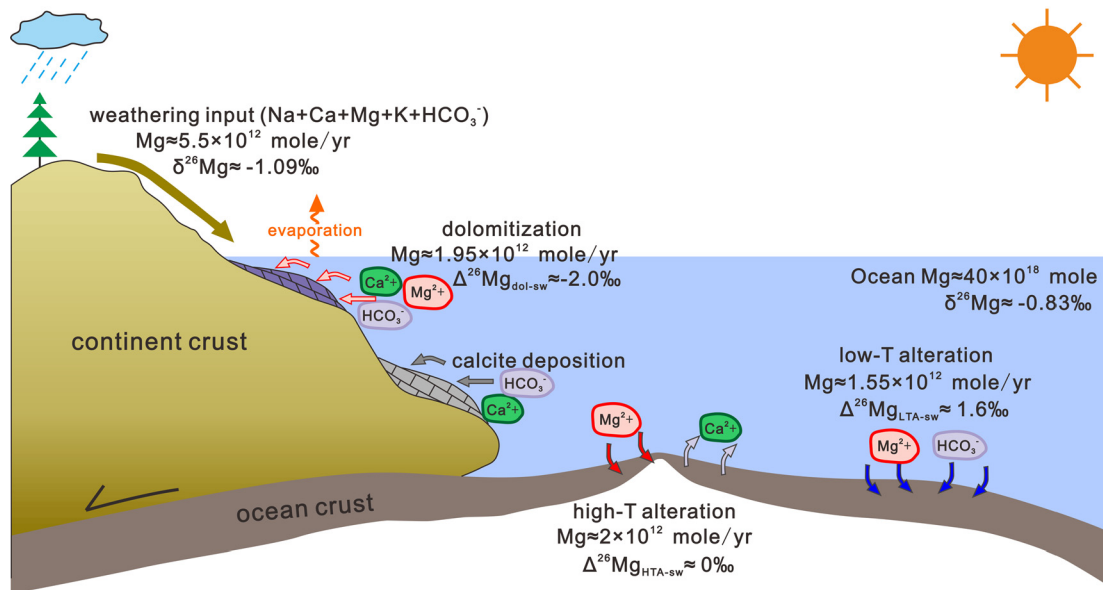


**Fig. 5.** Cartoon showing the steady-state Mg global cycles in the model. Numbers show the average fluxes and isotopic compositions of the main oceanic sources and sinks of Mg in the global Mg cycle during the late Cenozoic. The directions of the arrows refer to the net uptake or release of Mg, Ca, and alkalinity for each geological process.

### 4.3. Mg isotope constraints on global Mg cycling since the Neogene

#### 4.3.1. Numerical model of seawater chemistry

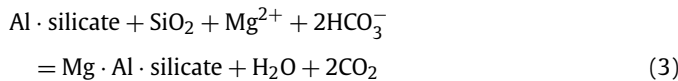
The rapid rise in seawater Mg contents implies a long-term imbalance in the global Mg cycle during the Cenozoic; however, the remarkably constant  $\delta^{26}\text{Mg}_{\text{sw}}$  throughout the late Cenozoic suggests a strong stabilizing mechanism for seawater Mg isotope compositions, which places a powerful new constraint on our understanding of the global Mg cycle over the past 23 Myr. In order to quantitatively analyze the responses and sensitivities of seawater Mg contents and isotopic compositions to changes in different Mg fluxes, we constructed a numerical model of the Mg and Ca cycles, seawater alkalinity, and seawater Mg isotope compositions (Fig. 5).

Magnesium isotope compositions ( $\delta^{26}\text{Mg}_{\text{sw}}$ ) and the mass of Mg ( $N_{\text{Mg}}$ ) in seawater are controlled by the influx of Mg in riverine runoff ( $F_{\text{riv}}$ ) into the ocean and outfluxes of Mg through high-temperature alteration at mid-ocean ridges ( $F_{\text{HTA}}$ ), dolomite precipitation ( $F_{\text{dol}}$ ), and low-temperature alteration and marine authigenic clay formation ( $F_{\text{MAC}}$ ) (Fig. 5; Higgins and Schrag, 2015; Li et al., 2015; Tipper et al., 2006). Following the Fantle and Tipper (2014), the dynamic changes in  $N_{\text{Mg}}$  and  $\delta^{26}\text{Mg}_{\text{sw}}$  can be described using the equations below:

$$\begin{aligned} \frac{dN_{\text{Mg}}}{dt} &= F_{\text{riv}} - F_{\text{HTA}} - F_{\text{dol}} - F_{\text{MAC}} \\ \frac{d\delta^{26}\text{Mg}_{\text{sw}}}{dt} &= (\delta^{26}\text{Mg}_{\text{riv}} - \delta^{26}\text{Mg}_{\text{sw}}) \cdot F_{\text{riv}}/N_{\text{Mg}} \end{aligned} \quad (1)$$

$$\begin{aligned}
& - \Delta^{26}\text{Mg}_{\text{dol-sw}} \cdot F_{\text{dol}}/N_{\text{Mg}} \\
& - \Delta^{26}\text{Mg}_{\text{MAC-sw}} \cdot F_{\text{MAC}}/N_{\text{Mg}}
\end{aligned} \quad (2)$$

where  $\delta^{26}\text{Mg}_{\text{riv}}$  is the Mg isotope compositions of riverine input, and  $\Delta^{26}\text{Mg}_{\text{dol-sw}}$  and  $\Delta^{26}\text{Mg}_{\text{MAC-sw}}$  are the Mg isotope fractionation factors associated with dolomite precipitation and phyllosilicate/clay formation, respectively. Because in high-temperature hydrothermal alteration processes, the Mg isotope fractionation is negligible,  $\Delta^{26}\text{Mg}_{\text{HTA-sw}} \cdot F_{\text{HTA}}/N_{\text{Mg}}$  will be 0, thereby, we did not put it in the ultimate equation. Formation of Mg-bearing phyllosilicate/clay and dolomite can be described by the following reactions:



According to reactions (3) and (4), the Mg sinks of dolomitization and phyllosilicate/clay formation are associated with the consumption of bicarbonate ions ( $\text{HCO}_3^-$ ). Because the largest contributor to seawater alkalinity is carbonate alkalinity (Boudreau et al., 2019; Caves et al., 2016; Ridgwell and Zeebe, 2005; Turchyn and DePaolo, 2019), changes in the Mg flux due to dolomitization and authigenic clay formation could change seawater alkalinity (Boudreau et al., 2019; Caves et al., 2016); however, seawater alkalinity over the past 23 Myr is suggested to have been relatively stable at 1.7–2.3 mmole/kg (Boudreau et al., 2019). It has been argued that when the concentration of major cations or anions changes, the ocean system compensates through the production or dissolution of  $\text{CaCO}_3$ , buffering seawater chemistry and atmospheric  $\text{CO}_2$  (Ridgwell and Zeebe, 2005; Turchyn and DePaolo, 2019). Our model, therefore, assumes that when the flux of alkalinity into the oceans is increased by processes such as enhanced continental weathering or a decrease in bicarbonate ion consumption, a counter-flux of alkalinity out of the oceans via  $\text{CaCO}_3$  precipitation is induced to keep the constant  $\text{HCO}_3^-$  budget of the ocean, and vice versa (Fig. 5). This assumption leads to a link between the Mg–Ca cycle, seawater alkalinity, continental weathering, and marine authigenic mineral formation. The changes in the mass of Ca in seawater ( $N_{\text{Ca}}$ ) and alkalinity with time can be described by the following equations:

$$\frac{dN_{\text{Ca}}}{dt} = F_{\text{riv}} - F_{\text{dol}} - F_{\text{cal}} + F_{\text{HTA}} \quad (5)$$

$$\begin{aligned}
\frac{d\text{ALK}}{dt} &= 2F_{\text{Ca-weathering}} + 2F_{\text{Mg-weathering}} + F_{(\text{Na+K})\text{-weathering}} \\
&\quad - 2F_{\text{MAC}} - 2F_{\text{cal}} - 2F_{\text{Mg-dol}}
\end{aligned} \quad (6)$$

where  $F_{\text{cal}}$  is the Ca outflux via pelagic carbonate deposition, and  $F_{\text{Ca-weathering}}$ ,  $F_{\text{Mg-weathering}}$ , and  $F_{(\text{Na+K})\text{-weathering}}$  are the Ca, Mg, and (Na+K) influxes from weathering, respectively.

A dynamic numerical model for seawater chemistry and Mg isotope composition can be constructed using the equations above.  $F_{\text{riv}}$ ,  $F_{\text{HTA}}$ ,  $F_{\text{dol}}$  and  $F_{\text{MAC}}$  are the tunable model parameters that represent the dynamic nature of the Mg–Ca mass balance in the model. Details of the model are provided in Appendix. By adjusting these parameters, we can obtain model outputs for different theoretical scenarios, which are compared with the measured Mg contents and isotopic compositions of seawater. For model benchmarking, we reproduced all four scenarios presented by Higgins and Schrag (2015) using the parameters provided, which validate our numerical model (Appendix Fig. S3-2).

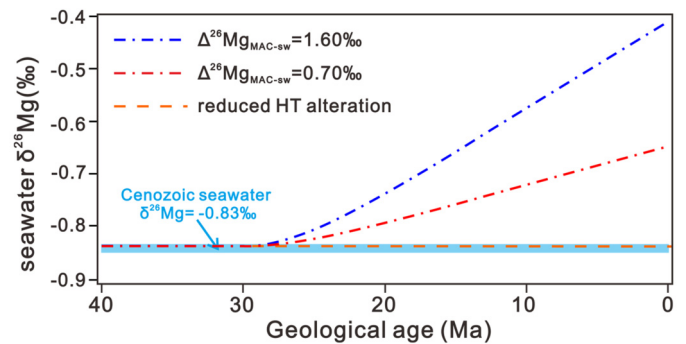


**Fig. 6.** Test of the sensitivity of seawater  $\delta^{26}\text{Mg}$  to changes in fluxes in high-temperature alteration, and Mg isotope fractionation factors associated with clay formations. The orange dashed line shows  $\delta^{26}\text{Mg}_{\text{sw}}$  values when the Mg outflux due to high-temperature (HT) alteration is reduced by 3 Tmole/y over the last 40 Myr. Blue and red dash-dot lines show the  $\delta^{26}\text{Mg}_{\text{sw}}$  values when Mg outflux due to low-temperature (LT) marine clay formation decreased from 5 to 2 Tmole/y since the late Cenozoic.  $\Delta^{26}\text{Mg}_{\text{MAC-sw}}$  is the Mg isotope fractionation factor between marine clay and seawater; the value proposed by Shalev et al. (2019) is  $\sim 1.6\text{‰}$  (blue dash-dot line) and the value proposed by Higgins and Schrag (2015) is  $0.7\text{‰}$  (red dash-dot line).

#### 4.3.2. Mechanisms accounting for the Cenozoic Seawater Conundrum

The quantitative removal of Mg from seawater during high-temperature hydrothermal alteration at mid-ocean ridges is not associated with Mg isotope fractionation (Teng, 2017), thus a decrease in the high-temperature alteration of oceanic crust could account for the rise in seawater Mg content with relatively stable  $\delta^{26}\text{Mg}_{\text{sw}}$  values (Fig. 6, orange dash line and Fig. S3-1 in the Appendix). However, the rate of oceanic and continental plate production has remained constant around  $\sim 3.4 \text{ km}^2/\text{y}$  over the last 40 Myr (Cogné and Humler, 2004; Rowley, 2002), ruling out decreased hydrothermal activity at mid-ocean ridges as the cause of the Cenozoic Seawater Conundrum. In contrast, orogenesis, atmospheric  $\text{CO}_2$  contents, and surface temperatures fluctuated significantly during the late Cenozoic (Li and Elderfield, 2013; Raymo and Ruddiman, 1992), leading to large changes in the rates of continental weathering, carbonate deposition, and low-temperature alteration of the oceanic crust (Caves et al., 2016; Higgins and Schrag, 2015; Li and Elderfield, 2013; Li and West, 2014). Therefore, the decoupling of changes in seawater Mg content and  $\delta^{26}\text{Mg}_{\text{sw}}$  during the late Cenozoic was most likely regulated by changes in riverine input, marine dolomitization, and phyllosilicate/clay formation.

Recent studies have suggested that the outflux of Mg into the modern oceanic crust via low-temperature alteration equates 12%–40% of the riverine input of Mg into oceans (Dunlea et al., 2017; Huang et al., 2018; Shalev et al., 2019), highlighting the importance of fluxes related to the formation of secondary silicate minerals in regulating the Mg isotope mass balance of seawater. The drop in seafloor temperature during Cenozoic cooling and the decrease in delivery of silica to the seafloor potentially caused a decrease in the rate of formation of marine authigenic clay, leading to an increase in the Mg content of seawater (Dunlea et al., 2017; Higgins and Schrag, 2015). Higgins and Schrag (2015) calculated that the Mg outflux caused by phyllosilicate/clay formation would have decreased by 3 Tmole/y (i.e., from 5 to 2 Tmole/y) to account for the observed increase in the Mg content of seawater during the Cenozoic. However, seawater  $\delta^{26}\text{Mg}$  values would increase by  $\sim 0.2\text{‰}$  over 40 Myr in this scenario (Higgins and Schrag, 2015), such variation was not resolvable using previous  $\delta^{26}\text{Mg}_{\text{sw}}$  archives (i.e., biogenic calcite or aragonite) because of their large uncertainty ( $\sim 0.4\text{‰}$ ). It should be noted that the Mg isotope fractionation factor between phyllosilicate/clay and seawater used by Higgins and Schrag (2015) was relatively small ( $\Delta^{26}\text{Mg}_{\text{MAC-sw}} = 0.7\text{‰}$ ; Fig. 6, red dashed line), yet a more recent study has proposed a  $\Delta^{26}\text{Mg}_{\text{MAC-sw}}$  factor of



**Table 1**  
Parameters of the box model for Mg cycling in seawater.

Initial parameters	Value	Reference
Total Mg amount of seawater, mole	$4 \times 10^{19}$ mole	Horita et al. (2002)
Seawater $\delta^{26}\text{Mg}$	-0.83‰	
Riverine input Mg amount	$5.5 \times 10^{12}$ mole/yr	
$\Delta^{26}\text{Mg}_{\text{dol-sw}}$	-2.0‰	Higgins and Schrag (2015), Li et al. (2015)
$\Delta^{26}\text{Mg}_{\text{MAC-sw}}$	1.6‰	Shalev et al. (2019)
$\delta^{26}\text{Mg}$ value of riverine input	-1.09‰	Tipper et al. (2006)
Mg flux in dolomitization	$1.95 \times 10^{12}$ mole/yr	Dunlea et al. (2017), Huang et al. (2018), Shalev et al. (2019)
Mg flux in marine autogenetic clay formation (MAC)	$1.55 \times 10^{12}$ mole/yr	
Mg flux in the MOR process (HTA)	$2 \times 10^{12}$ mole/yr	

1.6‰ (Shalev et al., 2019). If we run a numerical model where the Mg outflux via clay formation decreased by 3 Tmole/y since the late Cenozoic using a  $\Delta^{26}\text{Mg}_{\text{MAC-sw}}$  value of 1.6‰, the modeled  $\delta^{26}\text{Mg}_{\text{sw}}$  would increase by 0.4‰ over 20 Myr (Fig. 6, blue dashed line). These results are inconsistent with the observation from the XK-1 core, which shows constant  $\delta^{26}\text{Mg}_{\text{sw}}$  values since the late Cenozoic; therefore, an additional decrease in an Mg outflux that has a low  $\delta^{26}\text{Mg}$  value, or an increase in low- $\delta^{26}\text{Mg}$  influx into the ocean, or both, are required to counter-balance the isotopic effect of a reduction in Mg removal from seawater by the formation of phyllosilicate/clay.

Dolomitization is an important sink for Mg in seawater that preferentially removes light Mg isotopes, whereas riverine runoff is an important Mg input that has average  $\delta^{26}\text{Mg}$  values that are lower than that of seawater (Fig. 5). Therefore, the decline of dolomitization intensity or the increase of riverine input can balance the Mg isotope effects caused by the drop of the phyllosilicate/clay formation on seafloor. Herein, two end-member scenarios are considered to explain the increase in seawater Mg content at constant  $\delta^{26}\text{Mg}_{\text{sw}}$  values: (1) a simultaneous reduction in Mg outfluxes by dolomitization and phyllosilicate/clay formation; and (2) an increase in the weathering rate coupled with a drop in phyllosilicate/clay formation. These two scenarios can be tested using our numerical model.

We first set an initial chemical and isotopic steady-state for the Mg in the seawater in the model, then changed the influxes and outfluxes according to the two end-member scenarios and monitored the chemical and isotopic responses of seawater in the model. The Mg fluxes at the initial steady state were derived from a self-consistent steady-state isotopic and chemical mass balance calculation that assumed a constant influx of riverine Mg of 5.5 Tmole/y with a mean  $\delta^{26}\text{Mg}$  value of -1.09‰ and the updated Mg isotope fractionation factors listed in Table 1. In the steady-state model, the Mg outfluxes due to dolomitization, authigenic clay production, and high-temperature hydrothermal alteration are calculated to be 1.95, 1.55, and 2.00 Tmole/y, respectively (Table 1). These values are within the range of estimates from recent studies (Table 1). We then introduced perturbations to the steady-state system according to the two scenarios (details in the Appendix 3).

To increase the Mg content of seawater from 40 to 55 mM/kg in scenario 1 while maintaining a constant seawater  $\delta^{26}\text{Mg}$  value, the rates of dolomitization and low-temperature clay formation need to decrease by factors of 0.2 and 0.45, respectively (Fig. 7A), and the seawater alkalinity would increase by 30 mM/kg owing to the decreased consumption of  $\text{HCO}_3^-$ . To balance the seawater alkalinity,  $\text{CaCO}_3$ -carbonate production would increase, which would cause the seawater Ca content to decrease from 20 to 11 mM/kg (Fig. 7C) and the seawater Mg/Ca ratio to increase from 2 to 5.2 (Fig. 7D). These results match the seawater chemical compositions reconstructed from multiple geological archives, including halite

fluid inclusions, carbonate veins in the oceanic crust, and deep-sea pore fluid profiles (Fig. 7C–7D). It should also be noted that the modeled Mg fluxes caused by dolomitization and low-temperature authigenic clay formation in the model output are consistent with recent estimates for the modern ocean (Fig. 7A).

For scenario 2, we assume that the Mg outflux by dolomitization and the  $\delta^{26}\text{Mg}$  value of riverine input remained constant (Fig. 7E, Appendix 3). To reproduce the observed increase in seawater Mg contents and stable  $\delta^{26}\text{Mg}_{\text{sw}}$  values, the Mg flux caused by riverine input needs to increase by 14%, and the Mg outflux due to phyllosilicate/clay formation needs to decrease by 16% (Fig. 7E). However, in this case, the influx of  $\text{Ca}^{2+}$  would also increase significantly. Only when the additional Ca ions and alkalinity from the increased continental weathering were removed as carbonate, the modeled variation in the seawater Mg/Ca ratio could match the observed data (Fig. 7G–7H, the ideal curve). Otherwise, the seawater Ca contents would increase by a factor of 1.5, causing a decrease in seawater Mg/Ca ratios (Fig. 7G–7H, the green dash line).

We note that the two scenarios tested above are end-member scenarios; in reality all of these processes (decrease in dolomitization, decrease in clay formation, increase in riverine input) likely took place and contributed to the chemical and isotopic responses of seawater in the late Cenozoic. Nonetheless, the modeling results suggest that the stability of  $\delta^{26}\text{Mg}_{\text{sw}}$  values despite a dramatic increase in seawater Mg/Ca ratios cannot be driven solely by a decrease in the formation of clay on the seafloor; instead, multiple processes with similar effects on seawater elemental budget but opposite effects on  $\delta^{26}\text{Mg}_{\text{sw}}$  need to be coupled to explain the Cenozoic Seawater Conundrum.

#### 4.4. Implications for the global Mg–C cycle and the climate since the Cenozoic

The decline in atmospheric  $\text{CO}_2$  contents, which was commonly ascribed to enhanced continental weathering in response to the rise of the Tibetan plateau, resulted in global cooling during the Cenozoic (Raymo and Ruddiman, 1992). This long-term cooling over the past 65 Myr profoundly affected marine sediments and seawater chemistry (Boudreau et al., 2019; Higgins and Schrag, 2015). The development of continental icesheets and polar ice caps as a consequence of the Cenozoic cooling drove a  $\sim 100$  m fall in sea level since the early Eocene (Müller et al., 2008). Such variation significantly decreased the area of shallow carbonate platforms where dolomitization could occur (Warren, 2000). The drop in sea surface temperatures also slowed the rate of dolomitization in marine environments (Budd, 1997; Warren, 2000). The decline in pervasive dolomitization in marine environments since the Cretaceous has been noted in recent studies (Li et al., 2021). In addition, the rate of water–rock reactions during low-temperature alteration of the upper oceanic crust is also temperature depen-

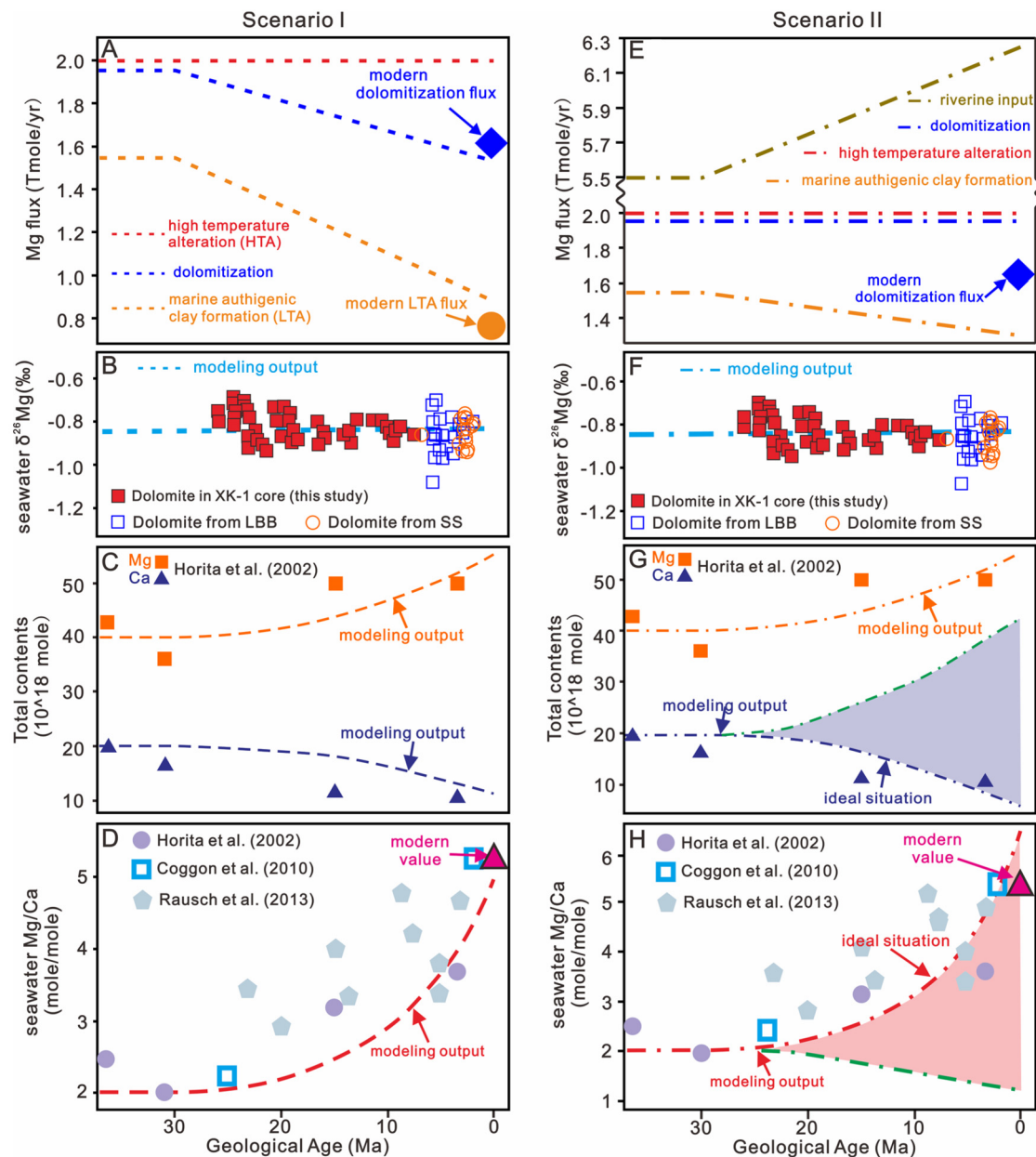


**Fig. 7.** Responses of  $\delta^{26}\text{Mg}_{\text{sw}}$  and Mg and Ca contents to (A–D) a decrease in the rate of dolomitization alongside a reduction in the rate of formation of marine authigenic clay (scenario 1) and (E–H) an increase in the rate of continental weathering alongside a reduction in the rate of formation of marine authigenic clay (scenario 2).

dent (Brady and Gíslason, 1997; Coggon et al., 2010; Higgins and Schrag, 2015). The decrease of seafloor temperature would lead to a significant reduction in Mg outflux of low-temperature fluid-rock reactions (Higgins and Schrag, 2015). In addition, biogenic Si is the key reactant for the formation of authigenic clay on seafloor (Michalopoulos and Aller, 2004), and the Cenozoic cooling suppressed the accumulation of biogenic silica and its diagenetic products (Dunlea et al., 2017). The drop in seafloor temperature and decline in the supply of reactive silica in response to global cooling, therefore, caused a reduction in phyllosilicate/clay formation (Dunlea et al., 2017; Gothmann et al., 2017; Higgins and Schrag, 2015).

During the Cenozoic, a combination of enhanced continental denudation, global cooling, and a reduction in dolomitization and phyllosilicate/clay formation should have regulated the global Mg cycle. Continental denudation drove Cenozoic cooling, and global cooling triggered a concurrent reduction in the Mg outflux from

the ocean owing to both dolomitization and phyllosilicate/clay formation, and as the two Mg sinks had an opposite effect on Mg isotope fractionation, they canceled each other and resulted in the stability in the  $\delta^{26}\text{Mg}$  values of the oceans over the past 23 Myr (Fig. 8).

The assumption in our model of stable seawater alkalinity as well as the rapid response of pelagic carbonate deposition to the perturbation of seawater alkalinity, is consistent with geological observations (Boudreau et al., 2019). Otherwise, the dramatic increase in the alkalinity of the oceans owing to the reduced Mg outflux via dolomitization and phyllosilicate/clay formation would have led to more  $\text{CO}_2$  in the atmosphere being converted into  $\text{CO}_3^{2-}$  in the ocean and accelerate the global cooling (Ridgwell and Zeebe, 2005; Turchyn and DePaolo, 2019). This implies that the increased pelagic  $\text{CaCO}_3$  preservation during the Cenozoic acted as an important negative feedback mechanism to maintain the atmospheric  $\text{CO}_2$  level.

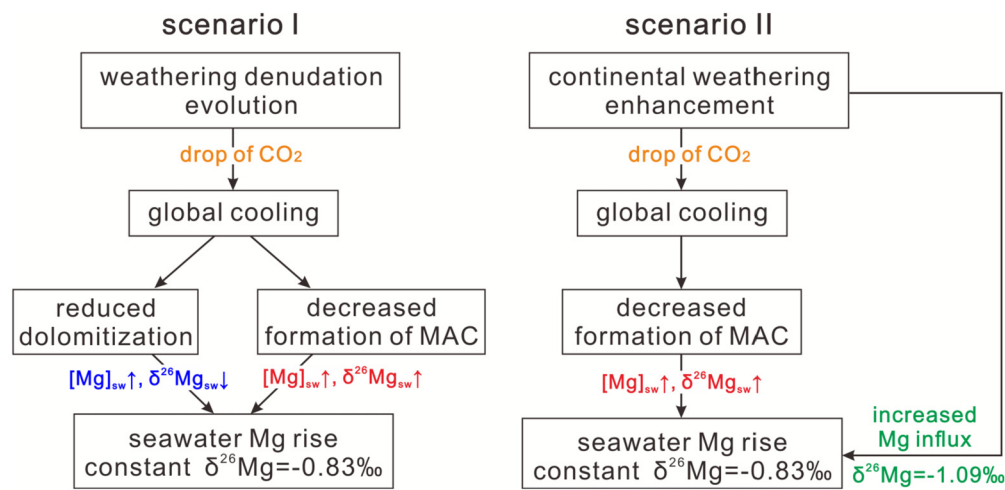


**Fig. 8.** Coupling of continental denudation, dolomitization, and marine authigenic clay formation in the context of global cooling and the effects on seawater Mg contents and  $\delta^{26}\text{Mg}$  values.

## 5. Conclusions

We performed high-density Mg isotope analyses of dolostones from the Xike-1 drill core, which recovered carbonates that were deposited in a tropical island setting during the late Cenozoic. Paleomagnetic, mineralogical, elemental and isotopic data from the carbonates suggest a syn-depositional origin for the dolostones in the Xike-1 core. The  $\delta^{26}\text{Mg}$  values of the dolostones range between  $-2.95\text{‰}$  and  $-2.71\text{‰}$ , which constrain the  $\delta^{26}\text{Mg}_{\text{sw}}$  value to a constant value around  $-0.83\text{‰}$  over the past 23 Myr, despite the rapid increase in seawater Mg/Ca ratios and Mg contents during the late Cenozoic. Numerical modelings suggest that this contrast between the Mg elemental and isotopic budgets of the oceans during the late Cenozoic was controlled by coupling of multiple processes, including decrease in the rates of both clay formation and dolomitization on the seafloor, and increase in the rate of continental weathering. This study suggests that the rise in the Mg contents of seawater and the stability of  $\delta^{26}\text{Mg}_{\text{sw}}$  values are driven by climatic changes with tectonic forcing. Furthermore, the assumption behind the modeling of the invariability of seawater alkalinity implies that the ocean system responded to the perturbation in seawater Mg chemistry through increased preservation of  $\text{CaCO}_3$ , which acted as a negative feedback to the decrease in atmospheric  $\text{CO}_2$ .

## CRediT authorship contribution statement

**Zhongya Hu:** XRD and isotope analysis, modeling, writing. **Zhiqiang Shi:** Sampling, petrography. **Gaojun Li:** discussion, revision. **Zhiguang Xia:** isotope analysis, revision. **Liang Yi:** Sampling. **Chuan Liu:** isotope analysis, revision. **Weiqliang Li:** Project design, funding acquisition, writing.

## Declaration of competing interest

The authors declare that they have no known competing financial interests or personal relationships that could have appeared to influence the work reported in this paper.

## Data availability

Data will be made available on request.

## Acknowledgements

This study is supported by the National Science Foundation of China (grants 42103004, 41873004, 41991324) and the China Postdoctoral Science Foundation (2020M681379). WL was supported by the Research Funds for the Frontiers Science Center for Critical Earth Material Cycling, Nanjing University. This work benefits from discussions with Shilei Li on geochemical models. Constructive comments from reviewers A. Immenhauser and M. Fantle and editor A. Jacobson greatly improved the manuscript.

## Appendix A. Supplementary material

Supplementary material related to this article can be found online at <https://doi.org/10.1016/j.epsl.2022.117755>.

## References

- Ahm, A.-S.C., Bjerrum, C.J., Blättler, C.L., Swart, P.K., Higgins, J.A., 2018. Quantifying early marine diagenesis in shallow-water carbonate sediments. *Geochim. Cosmochim. Acta* 236, 140–159.
- Bi, D.J., Zhai, S.K., Zhang, D.J., Liu, X.F., Liu, X.Y., Jiang, L.J., Zhang, A.B., 2018a. Constraints of fluid inclusions and C, O isotopic compositions on the origin of the dolomites in the Xisha Islands, South China Sea. *Chem. Geol.* 493, 504–517.
- Bi, D., Zhang, D., Zhai, S., Liu, X., Xiu, C., Liu, X., Jiang, L., Zhang, A., Li, S., 2018b. Seawater  $^{87}\text{Sr}/^{86}\text{Sr}$  values recorded by reef carbonates from the Xisha Islands (South China Sea) since the Neogene and its response to the uplift of Qinghai-Tibetan Plateau. *Geo. J.* 54, 3878–3890.
- Bialik, O.M., Wang, X., Zhao, S., Waldmann, N.D., Frank, R., Li, W., 2018. Mg isotope response to dolomitization in hinterland-attached carbonate platforms: outlook of  $\delta^{26}\text{Mg}$  as a tracer of basin restriction and seawater Mg/Ca ratio. *Geochim. Cosmochim. Acta* 235, 189–207.
- Boudreau, B.P., Middelburg, J.J., Sluijs, A., van der Ploeg, R., 2019. Secular variations in the carbonate chemistry of the oceans over the Cenozoic. *Earth Planet. Sci. Lett.* 512, 194–206.
- Brady, P.V., Gislason, S.R., 1997. Seafloor weathering controls on atmospheric  $\text{CO}_2$  and global climate. *Geochim. Cosmochim. Acta* 61, 965–973.
- Budd, D.A., 1997. Cenozoic dolomites of carbonate islands: their attributes and origin. *Earth-Sci. Rev.* 42, 1–47.
- Caves, J.K., Jost, A.B., Lau, K.V., Maher, K., 2016. Cenozoic carbon cycle imbalances and a variable weathering feedback. *Earth Planet. Sci. Lett.* 450, 152–163.
- Chang, B., Li, C., Liu, D., Foster, I., Tripati, A., Lloyd, M.K., Maradiaga, I., Luo, G., An, Z., She, Z., Xie, S., Tong, J., Huang, J., Algeo, T.J., Lyons, T.W., Immenhauser, A., 2020. Massive formation of early diagenetic dolomite in the Ediacaran ocean: constraints on the “dolomite problem”. *Proc. Natl. Acad. Sci. USA* 117 (25), 14005–14014.
- Cioppa, M.T., Al-Aasm, I.S., Symons, D.T.A., Gillen, K.P., 2003. Dating penecontemporaneous dolomitization in carbonate reservoirs: paleomagnetic, petrographic, and geochemical constraints. *AAPG Bull.* 87, 77–88.

- Coggon, R.M., Teagle, D.A., Smithduque, C.E., Alt, J.C., Cooper, M.J., 2010. Reconstructing past seawater Mg/Ca and Sr/Ca from mid-ocean ridge flank calcium carbonate veins. *Science* 327, 1114–1117.
- Cogné, J.P., Humler, E., 2004. Temporal variation of oceanic spreading and crustal production rates during the last 180 My. *Earth Planet. Sci. Lett.* 227 (3–4), 427–439.
- Dunlea, A.G., Murray, R.W., Santiago Ramos, D.P., Higgins, J.A., 2017. Cenozoic global cooling and increased seawater Mg/Ca via reduced reverse weathering. *Nat. Commun.* 8.
- Fantle, M.S., Barnes, B.D., Lau, K.V., 2020. The role of diagenesis in shaping the geochemistry of the marine carbonate record. *Annu. Rev. Earth Planet. Sci.* 48, 549–583.
- Fantle, M.S., Higgins, J., 2014. The effects of diagenesis and dolomitization on Ca and Mg isotopes in marine platform carbonates: implications for the geochemical cycles of Ca and Mg. *Geochim. Cosmochim. Acta* 142, 458–481.
- Fantle, M.S., Tipper, E.T., 2014. Calcium isotopes in the global biogeochemical Ca cycle: implications for development of a Ca isotope proxy. *Earth-Sci. Rev.* 129, 148–177.
- Geske, A., Goldstein, R.H., Mavromatis, V., Richter, D.K., Immenhauser, A., 2015. The magnesium isotope ( $\delta^{26}\text{Mg}$ ) signature of dolomites. *Geochim. Cosmochim. Acta* 149, 131–151.
- Geske, A., Zorlu, J., Richter, D.K., Buhl, D., Niedermayr, A., Immenhauser, A., 2012. Impact of diagenesis and low grade metamorphism on isotope ( $\delta^{26}\text{Mg}$ ,  $\delta^{13}\text{C}$ ,  $\delta^{18}\text{O}$  and  $^{87}\text{Sr}/^{86}\text{Sr}$ ) and elemental (Ca, Mg, Mn, Fe and Sr) signatures of Triassic sabkha dolomites. *Chem. Geol.* 332–333, 45–64.
- Gothmann, A.M., Stolarski, J., Adkins, J.F., Higgins, J.A., 2017. A Cenozoic record of seawater Mg isotopes in well-preserved fossil corals. *Geology* 45, 1039–1042.
- Higgins, J.A., Blättler, C.L., Lundstrom, E.A., Santiago-Ramos, D.P., Akhtar, A.A., Crüger Ahm, A.S., Bialik, O., Holmden, C., Bradbury, H., Murray, S.T., Swart, P.K., 2018. Mineralogy, early marine diagenesis, and the chemistry of shallow-water carbonate sediments. *Geochim. Cosmochim. Acta* 220, 512–534.
- Higgins, J.A., Schrag, D.P., 2015. The Mg isotopic composition of Cenozoic seawater – evidence for a link between Mg-clays, seawater Mg/Ca, and climate. *Earth Planet. Sci. Lett.* 416, 73–81.
- Horita, J., Zimmermann, H., Holland, H., 2002. Chemical evolution of seawater during the Phanerozoic: implications from the record of marine evaporites. *Geochim. Cosmochim. Acta* 66, 3733–3756.
- Hu, Z., Li, W., Zhang, H., Krainer, K., Zheng, Q.F., Xia, Z., Hu, W., Shen, S.Z., 2021. Mg isotope evidence for restriction events within the Paleotethys ocean around the Permian-Triassic transition. *Earth Planet. Sci. Lett.* 556, 116704.
- Huang, K.J., Teng, F.Z., Plank, T., Staudigel, H., Hu, Y., Bao, Z.Y., 2018. Magnesium isotopic composition of altered oceanic crust and the global Mg cycle. *Geochim. Cosmochim. Acta* 238, 357–373.
- Immenhauser, A., 2021. On the delimitation of the carbonate burial realm. *Depos. Rec.*
- Jacobson, A.D., Zhang, Z., Lundstrom, C., Huang, F., 2010. Behavior of Mg isotopes during dedolomitization in the Madison Aquifer, South Dakota. *Earth Planet. Sci. Lett.* 297, 446–452.
- Li, W., Beard, B.L., Li, C., Xu, H., Johnson, C.M., 2015. Experimental calibration of Mg isotope fractionation between dolomite and aqueous solution and its geological implications. *Geochim. Cosmochim. Acta* 157, 164–181.
- Li, G., Elderfield, H., 2013. Evolution of carbon cycle over the past 100 million years. *Geochim. Cosmochim. Acta* 103, 11–25.
- Li, G., West, A.J., 2014. Evolution of Cenozoic seawater lithium isotopes: coupling of global denudation regime and shifting seawater sinks. *Earth Planet. Sci. Lett.* 401, 284–293.
- Li, M., Wignall, P.B., Dai, X., Hu, M., Song, H., 2021. Phanerozoic variation in dolomite abundance linked to oceanic anoxia. *Geology* 49, 698–702.
- Liu, C., Wang, Z., Raub, T.D., Macdonald, F.A., Evans, D.A.D., 2014. Neoproterozoic cap-dolomite deposition in stratified glacial meltwater plume. *Earth Planet. Sci. Lett.* 404, 22–32.
- Lowenstein, T.K., Timofeeff, M.N., Brennan, S.T., Hardie, L.A., Demicco, R.V., 2001. Oscillations in Phanerozoic seawater chemistry: evidence from fluid inclusions. *Science* 294, 1086–1088.
- Michalopoulos, P., Aller, R.C., 2004. Early diagenesis of biogenic silica in the Amazon delta: alteration, authigenic clay formation, and storage. *Geochim. Cosmochim. Acta* 68, 1061–1085.
- McArthur, J.M., Howarth, R.J., Bailey, T.R., 2001. Strontium isotope stratigraphy: LOWESS version 3: best fit to the marine Sr-isotope curve for 0–509 Ma and accompanying look-up table for deriving numerical age. *J. Geol.* 109, 155–170.
- Müller, R.D., Sdrólías, M., Gaina, C., Steinberger, B., Heine, C., 2008. Long-term sea-level fluctuations driven by ocean basin dynamics. *Science* 319, 1357–1362.
- Pogge von Strandmann, P.A.E., Forshaw, J., Schmidt, D.N., 2014. Modern and Cenozoic records of seawater magnesium from foraminiferal Mg isotopes. *Biogeosciences* 11, 5155–5168.
- Raymo, M.E., Ruddiman, W.F., 1992. Tectonic forcing of late Cenozoic climate. *Nature* 359, 117–122.
- Ridgwell, A., Zeebe, R., 2005. The role of the global carbonate cycle in the regulation and evolution of the Earth system. *Earth Planet. Sci. Lett.* 234, 299–315.
- Rowley, D.B., 2002. Rate of plate creation and destruction: 180 Ma to present. *Geol. Soc. Am. Bull.* 114, 927–933.
- Saenger, C., Wang, Z., 2014. Magnesium isotope fractionation in biogenic and abiogenic carbonates: implications for paleoenvironmental proxies. *Quat. Sci. Rev.* 90, 1–21.
- Shalev, N., Bontognali, T.R., Wheat, C.G., Vance, D., 2019. New isotope constraints on the Mg oceanic budget point to cryptic modern dolomite formation. *Nat. Commun.* 10, 1–10.
- Shao, L., Cui, Y., Qiao, P., Zhang, D., Liu, X., Zhang, C., 2017. Sea-level changes and carbonate platform evolution of the Xisha Islands (South China Sea) since the Early Miocene. *Palaeogeogr. Palaeoclimatol. Palaeoecol.* 485, 504–516.
- Shi, Z., Xie, H., Liu, L., Zhang, D., You, L., 2016. The Sedimentology of Carbonate Reef Reservoir of Xi Ke 1 Core in South China Sea: Reservoir and Diagenesis, 1st ed. China University of Geoscience Press, Wuhan, China, pp. 53–93 (in Chinese).
- Teng, F.Z., 2017. Magnesium isotope geochemistry. *Rev. Mineral. Geochem.* 82, 219–287.
- Tipper, E., Galy, A., Gaillardet, J., Bickle, M., Elderfield, H., Carder, E., 2006. The magnesium isotope budget of the modern ocean: constraints from riverine magnesium isotope ratios. *Earth Planet. Sci. Lett.* 250, 241–253.
- Turchyn, A.V., DePaolo, D.J., 2019. Seawater chemistry through Phanerozoic time. *Annu. Rev. Earth Planet. Sci.* 47, 197–224.
- Wang, R., Yu, K., Jones, B., Wang, Y., Zhao, J., Feng, Y., Bian, L., Xu, S., Fan, T., Jiang, W., Zhang, Y., 2018. Evolution and development of Miocene “island dolostones” on Xisha Islands, South China Sea. *Mar. Geol.* 406, 142–158.
- Warren, J., 2000. Dolomite: occurrence, evolution and economically important associations. *Earth-Sci. Rev.* 52, 1–81.
- Wilkinson, B.H., Algeo, T.J., 1989. Sedimentary carbonate record of calcium-magnesium cycling. *Am. J. Sci.* 289, 1158–1194.
- Yi, L., Jian, Z., Liu, X., Zhu, Y., Zhang, D., Wang, Z., Deng, C., 2018. Astronomical tuning and magnetostratigraphy of Neogene biogenic reefs in Xisha Islands, South China Sea. *Sci. Bull.* 63, 564–573.